

Solar Energetic Particle Forecasting with Multi-Task Deep Learning: SEPNet

**Yian Yu¹, Yang Chen¹, Lulu Zhao², Kathryn Whitman³, Ward Manchester²,
Tamas Gombosi²**

¹Department of Statistics, University of Michigan, Ann Arbor, MI, USA

²Department of Climate and Space Sciences and Engineering, University of Michigan, Ann Arbor, MI,
USA

³NASA Space Radiation Analysis Group, Johnson Space Center, Houston, TX, USA

Key Points:

- We propose a multi-task deep learning model, SEPNet, for SEP prediction.
- SEPNet predicts SEP events using solar flare data and solar magnetic field measurements from SDO.
- SEPNet outperforms classical machine learning models in giving earlier and more reliable SEP alerts, especially when employing solar magnetic field measurement as predictors.

Abstract

Solar energetic particle (SEP) events pose severe threats to spacecraft, astronaut safety, and aviation operations, accurate SEP forecasting remains a critical challenge in space weather research due to their complex origins and highly variable propagation. In this work, we built SEPNet, an innovative multi-task neural network that jointly predicts future solar eruptive events, including solar flares and coronal mass ejections (CMEs) and SEPs, incorporating long short-term memory and transformer architectures that capture contextual dependencies. SEPNet is a machine learning framework for SEP prediction that utilizes an extensive set of predictors, including solar flares, CMEs, and space-weather HMI active region patches (SHARP) magnetic field parameters. SEPNet is rigorously evaluated on the SEPVAL SEP dataset ((Whitman, 2025b)), which is used to evaluate the performance of the current SEP prediction models. The performance of SEPNet is compared with classical machine learning methods and current state-of-the-art pre-eruptive SEP prediction models. The results show that SEPNet, particularly with SHARP parameters, achieves higher detection rates and skill scores while maintaining suitable for real-time space weather alert operations. Although class imbalance in the data leads to relatively high false alarm rates, SEPNet consistently outperforms reference methods and provides timely SEP forecasts, highlighting the capability of deep multi-task learning for next-generation space weather prediction. All data and code are available on GitHub at <https://github.com/yuyian/SEP-Prediction.git>.

Plain Language Summary

Explosions on the Sun can send high-energy particles, called solar energetic particles (SEPs), into space. SEP events are a type of solar radiation storm that can affect astronauts, satellites, and high-latitude aircraft because the particles can damage the electronics and pose a safety risk to humans. In this work, we presented SEPNet, a new computer tool that uses solar eruptive events, including solar flares and the measurement of the solar magnetic fields, to predict when SEP events will occur. SEPNet uses artificial intelligence to learn from past space weather data and provides better early warnings than current existing methods. SEPNet shows promise in helping scientists and decision-makers protect us from the risks of space weather.

1 Introduction

Solar energetic particle (SEP) events are transient releases of high-energy protons, electrons, and heavy ions accelerated during solar flares and coronal mass ejections (CMEs) (Hilberg, 1969; Iucci et al., 2005). These charged particles constitute significant radiation hazards to spacecraft electronics, astronaut safety, and high-latitude aviation operations (Eastwood et al., 2017; Whitman et al., 2023). As human activities extend beyond low Earth orbit, accurate real-time forecasting of SEP events has become increasingly vital yet remains challenging due to their intermittent occurrence and the complex mechanisms underlying particle acceleration and interplanetary transport (Kim et al., 2011; Reames, 2004; M. Desai & Giacalone, 2016; Klein & Dalla, 2017). Over recent decades, SEP prediction has progressed across empirical, physics-based, and machine learning methods, aiming to balance predictive accuracy with operational timeliness (Smart & Shea, 1979; Opgenoorth, Hermann J. et al., 2019; Kasapis et al., 2022; Ali et al., 2025).

Traditional SEP models generally integrates physical understanding of particle acceleration at solar flares and CME-shocks with solar eruption observations through empirical relations or physics-based acceleration and transport simulations. Empirical models rely on statistical correlations derived from historical data to rapidly forecast SEP occurrence or intensity using flare, CME, and radio burst parameters, but may lack detailed physical interpretation (Smart & Shea, 1979; Balch, 2008; Laurenza et al., 2009). Physics-based models simulate the fundamental processes of SEP acceleration and trans-

port in the corona and heliosphere by coupling solar wind, CME shock evolution, and particle kinetics, often solving the transport equations and modeling diffusive shock acceleration (Luhmann et al., 2007; Sokolov et al., 2004; Hu et al., 2017; Zhao, 2023; W. Liu et al., 2025). Despite their interpretability and scientific value, these physics-based models tend to be computationally intensive and there are still uncertainties in key input parameters such as seed particle populations and accurate CME/shock characteristics (M. I. Desai et al., 2020; Tylka & Lee, 2006; Neergaard Parker & Zank, 2012). For empirically driven forecasting, additional observational constraints, such as delays in coronagraph data acquisition, limited real-time radio observations, and imperfect knowledge of magnetic connectivity to the observing spacecraft, also pose challenges for operational deployment (Richardson et al., 2014; Erickson, 1997; Gopalswamy et al., 2005). The trade-offs between physical completeness and operational practicality leads to a proliferation of varied model designs, each with advantages and limitations regarding forecast accuracy, timeliness, and interpretability (Whitman et al., 2023).

The growing availability of diverse, multiwavelength solar observational data, alongside advancements in machine learning (ML) techniques, has spurred numerous ML-based approaches for SEP forecasting (Whitman et al., 2023; Dayeh et al., 2024; Kasapis et al., 2022). ML models usually integrate features such as solar flare characteristics, CME parameters, and photospheric magnetic field descriptors like the space-weather HMI active region patches (SHARP). These models have demonstrated competitive or superior prediction performance compared to traditional empirical or physics-based models, achieving improved operational timeliness and accuracy. For instance, convolutional neural networks, support vector machines, and ensemble tree methods have been used to predict SEP occurrence probabilities and intensities by leveraging feature sets including flare X-ray flux, CME speed and width, and magnetic field proxies (Kasapis et al., 2022; Lavasa et al., 2021; Boubrahimi et al., 2017). Recent work by Ji et al. (2025) advances this field by proposing a novel framework that combines global feature mapping and multivariate time series classification to enhance model interpretability alongside accuracy. A notable limitation in previous ML models was the limited size and diversity of available SEP event datasets. For example, Kasapis et al. (2022) reported predictive accuracy of approximately 0.72 using a modest dataset of 65 SEP events, highlighting the critical need for larger, curated datasets spanning recent solar cycles for more robust model training and validation. Responding to this, the SEPVAL initiative established a collaborative, multi-year benchmark for SEP model validation by compiling and curating an extensive SEP event dataset, involving model developers, operational stakeholders, and the space weather research community (Whitman & Collaboration, 2024; Whitman et al., 2024). A detailed introduction to the SEPVAL dataset is provided in Section 2.1.1.

Departing from conventional single-task learning frameworks, multi-task learning models jointly learn related prediction tasks by sharing latent representations, which enhances generalization and mitigates overfitting especially in data-constrained environments (Caruana, 1997; Y. Zhang & Yang, 2017; Crawshaw, 2020). The inherently interconnected nature of solar eruptive phenomena, where flares, CMEs, and SEPs are physically and temporally coupled, naturally motivates multi-task learning approaches. To date, SEP prediction efforts have often treated SEP occurrence, flare forecasting, and CME characteristics as separate or sequential problems. However, joint modeling through multi-task learning can exploit shared underlying physics and temporal correlations, yielding more accurate and stable predictions.

In this work, we utilize a comprehensive, up-to-date dataset compiled through September 2025, encompassing detailed records of solar flares, CMEs, and SHARP magnetic field parameters together with a rigorously curated catalog of SEP events. This extensive dataset underpins the training of a novel multi-task learning model, SEPNet, which is designed to simultaneously predict SEP event occurrence and continuous flare and CME parameters. SEPNet employs shared neural network layers coupled with task-specific output

heads, effectively capturing the latent interdependencies inherent in solar eruptive phenomena. The model integrates temporal dynamics through recurrent long short-term memory (LSTM) (Hochreiter & Schmidhuber, 1997) and attention-based transformer (Vaswani et al., 2023) architectures, enabling the exploitation of sequential dependencies in solar observations and thereby enhancing predictive capabilities relative to traditional single-task classifiers.

The remainder of this paper is organized as follows. Section 2 details the methodology, including data preparation, preprocessing steps, and the development of the SEPNet model. Within this section, we describe the feature selection procedure and the strategies employed for model training and evaluation. In Section 3, we present the results of applying the SEPNet model and the update version SEPNet2 to the SEPVAL dataset, including a comparative analysis with conventional machine learning classifiers and real-time operational SEP prediction. Finally, Sections 4 and 5 discuss and summarize the main findings and conclusions of this study, and directions for future research. Additional details and supplementary tables that support the results are provided in the Appendix.

2 Methodology

A detailed description of the data preprocessing workflow is presented in Section 2.1. In Section 2.2, we introduce the model SEPNet designed to utilize shared layers to simultaneously predict both the future flare and CME features and the probability of the occurrence of a future SEP event. This structure enables the model to learn from correlations among all available solar activity data, combining future flare and CME information directly to improved SEP prediction performance.

To enhance practical applicability and improve the prediction of operational SEP events, we further refine the model architecture, and the results are presented in Section 3. The model is initially trained using all SEP event enhancements above GOES background, indicated by a proton flux threshold of 10^{-6} pfu in the CLEAR SEP benchmark dataset, which helps mitigate issues related to data imbalance and strengthens the robustness of model training. For operational deployment, samples labeled as operational SEP events (> 10 MeV proton flux > 10 pfu) are used as a validation set to fine-tune the classification threshold for distinguishing operational SEP events.

2.1 Data Preparation

The machine learning models developed in this study are designed for predictive tasks, necessitating two sources of input data: a feature set (predictors) and response variables. This section details the data sources and the preprocessing steps undertaken for model training and evaluation.

For the response variables, we use SEP records from the CLEAR SEP benchmark dataset provided by the `FetchSEP` (Whitman, 2025a) python module covering the period from 3 February 1986 to 10 September 2025. This dataset includes 568 general SEP events, defined as periods when proton flux in the >10 MeV channel exceeds background levels (indicated with a threshold 10^{-6} pfu). Among these, 267 events surpass the operational threshold of 10 pfu in the > 10 MeV proton channel, which is the criterion used by NOAA's Space Weather Prediction Center and NASA's Space Radiation Analysis Group to define a solar radiation storm or operational SEP event (see details in <https://www.swpc.noaa.gov/phenomena/solar-radiation-storm> and <https://srag.jsc.nasa.gov/spaceradiation/what/what.cfm>). Each event is characterized by the start and end times at which the > 10 MeV proton flux crosses the respective thresholds. Note that these events are relatively rare over such an extended time period, highlighting the challenge of data sparsity in SEP forecasting studies.

The feature data sources include solar flares and CMEs, as well as SHARP parameters. The flare dataset, derived from GOES measurements, spans from 1 September 1975 to 29 September 2025 and it includes a total of 88,492 flares. For each flare, we calculate its duration (time from start to end), the rise time (time from start to peak), and the logarithm of its peak flux. The CME events were obtained from the CCMC DONKI dataset covering the period from 3 April 2010 to 25 September 2025, totaling 7,507 events (available at <https://kauai.ccmc.gsfc.nasa.gov/DONKI/search/>). For each CME, we include the features of latitude, longitude, half angle, and speed. SHARP parameters, which are scalar quantities derived from full photospheric vector magnetic field magnetograms with a 12-minute cadence (see Bobra et al. (2014) for detailed methodology), are included as well. A subset of the SHARP parameters, including LAT MIN, LON MIN, LAT MAX, LON MAX, USFLUX, MEANGAM, MEANGBT, MEANGBZ, MEANGBH, MEANJZD, TOTUSJZ, MEANALP, MEANJZH, TOTUSJH, ABSNJZH, SAVNCPP, MEANPOT, TOTPOT, MEANSHR, SHRGT45, SIZE, SIZE ACR, NACR, and NPIX are included in our study. The SHARP dataset, provided by the Stanford Joint Science Operations Center (see <http://jsoc.stanford.edu/ajax/lookdata.html>) and accessed with the SunPy package drms (Community et al., 2020; Glogowski et al., 2019), ranges from 1 May 2010 to 30 September 2025 with a total of 2,632,097 records. For all three data sources (flare, CME, and SHARP), we use data limited to the time range beginning 24 hours prior to the start of the earliest SEP event and ending at the earliest of the latest available timestamp across all sources. The full set of SEP, flare, CME, and SHARP events utilized in this study is visualized in Figure 1.

The SHARP dataset provides condensed measurements at a 12-minute resolution. However, several features contain missing values except for USFLUX, TOTUSJZ, TOTUSJH, ABSNJZH, SAVNCPP, and TOTPOT during our download periods. For the remaining features with missing entries, we applied a k -nearest-neighbors imputation approach using $k = 10$. Missing values were estimated by computing the weighted average of the corresponding feature values from the identified nearest neighbors.

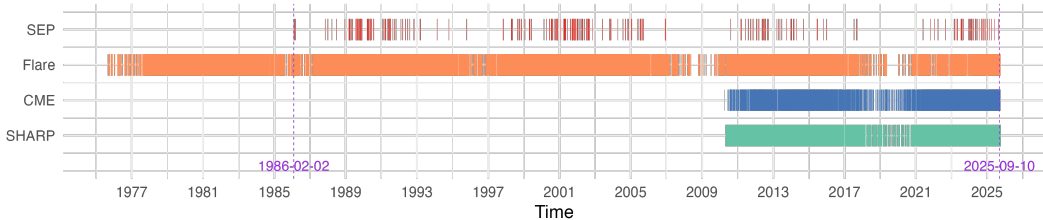


Figure 1. Timeline visualization of operational SEP (> 10 MeV 10 pfu), flare, CME, and SHARP records used in this study. For each data source, only records occurring between 24 hours before the first SEP event search time and the minimum of the latest recorded times across all sources are included. Each colored band marks the temporal occurrence of a record by type: operational SEP (red), flare (orange), CME (blue), and SHARP (green). Vertical dashed lines indicate the selected time period.

2.1.1 Data Preprocessing

In this study, we develop a prediction model that uses solar flare, CMEs, and SHARP parameters aggregated over 2 24-hour window to forecast the occurrence of SEP events in the subsequent 24 hours. We construct the training and testing datasets using a rolling window approach with fixed, non-overlapping 24-hour windows. For each window, we compute the minimum, maximum, and average values of all features from the flare, CME,

or SHARP records. For our multi-task learning model, we also predict the number of flare and CME events in the 24-hour forecast window and record these counts for subsequent analysis. After removing windows with all flare, CME, and SHARP data missing, the final dataset comprises 11,773 samples, including 3,537 samples labeled as positive for future general SEP occurrence, and within this subset, 1,726 samples are further labeled as future operational SEP occurrence.

Since we will evaluate model performance on the SEPVAL dataset, we use the designated periods specified in the SEPVAL dataset when constructing the testing set. The SEPVAL dataset is available on Zenodo at <https://doi.org/10.5281/zenodo.15020584> with supplementary resources provided at <https://ccmc.gsfc.nasa.gov/community-workshops/ccmc-sepval-2023/>. The SEPVAL dataset encompasses a total of 33 SEP and 30 non-SEP events spanning from 2011 to 2023. Notably, most non-SEP events have strong flares associated with them, adding further complexity to the challenge of distinguishing SEP from non-SEP intervals. We reserve 24-hour windows preceding each event in the SEPVAL dataset as the testing set, and use the remaining time windows for model training. To avoid unequal testing sample sizes and to retain physically meaningful quiet intervals when only flare or CME features are used across different feature selection scenarios, especially when no flare or CME is recorded in a given 24-hour window, we do not discard these samples or treat them as generic missing data. Instead, flare- and CME-related features are set to zero, and the logarithm of the flare peak flux is fixed to -10 to represent background or null activity (Winter & Balasubramaniam, 2015).

After splitting the data into training and testing samples, all input features were normalized to the range $[0, 1]$ using min-max scaling defined by $x' = (x - x_{\min}) / (x_{\max} - x_{\min})$, where x_{\min} and x_{\max} are the minimum and maximum values computed over the training set (Hastie et al., 2009). No information from the testing set is used in the normalization step.

2.1.2 Feature Selection

Given that significant correlations exist among SHARP parameters, CME properties, and solar flare characteristics, e.g., C. Liu et al. (2017) and Jiao et al. (2020), we systematically investigated different combinations of these feature groups to optimize predictive performance and mitigate overfitting risks. Due to different temporal coverage in the dataset (for example, SHARP parameters were not available prior to 2010), including specific variables as input features consequently alters the amount of usable data. Table 1 summarizes the data volume corresponding to general SEP and non-SEP labels for each feature subset. Notably, using flare data alone provides the largest sample size owing to its longest temporal coverage; however, subsequent results demonstrate that despite the greater volume, models trained solely on flare data exhibit suboptimal performance. For each candidate feature subset, the multi-task learning model was reinitialized and trained epoch-wise to ensure consistent evaluation.

Table 1. Data size across different feature sets.

	F	C	F+C	S	S+F	S + C	S+F+C
General SEP	3334	997	829	1260	1059	993	827
Non-SEP	7071	2232	1592	3550	2532	2042	1549

Features abbreviations: F = flare-related features, S = SHARP parameters, C = CME-related features.

2.2 Model Architecture

We developed a multi-task neural network model, SEPNet, to capture the complex relationship among solar flares, CMEs, and SHARP parameters in relation to SEP occurrences. By simultaneously learning to predict flare and CME features along with SEP events in a multi-task framework, SEPNet leverages the shared information across these related solar phenomena. This integrated approach enables the model to adaptively utilize predictive signals from flare and CME dynamics to improve the accuracy of SEP event forecasts within the next 24 hours.

The flowchart of the SEPNet model is depicted in the top panel of Figure 2. For each sample, the input consists of a set of min-max normalized features derived from solar flare, CME, and SHARP magnetic field data. These features are processed through three shared fully connected (dense) layers with gradually reduced feature dimensionality (from 256 to 128, 64, and 16), which encourages the formation of efficient, compressed representations and facilitating hierarchical feature extraction (Wang & Sun, 2024; Wu et al., 2020). Each dense layer is followed by layer normalization, which stabilizes training and mitigates issues arising from varying input data scales and is particularly beneficial for deep multilayer perceptrons. ReLU activation functions, $\text{ReLU}(x) = \max(x, 0)$, introduce nonlinearity (Zou et al., 2020). Dropout is applied after activation to prevent coadaptation of neurons and reduce overfitting risks. The staged compression helps filter noise and focuses network capacity, ensuring the final shared representation remains suitably compact for both tasks while balancing model complexity and computational efficiency.

The shared embedding is then fed into two distinct output heads to implement multi-task learning: a regression head that predicts the counts of future flare and CME events, and a classification head that outputs the predicted probability for the occurrence of a future SEP event. This architectural choice leverages feature sharing to boost learning efficiency while allowing task-specific prediction at the output layer (Sandnes et al., 2024).

To better capture temporal dependencies and complex sequential patterns in the input data, the updated model SEPNet2 integrates recurrent and attention mechanisms by combining a unidirectional LSTM layer with a transformer encoder, illustrated in the bottom panel of Figure 2. The input sequences first pass through the LSTM to extract dynamic sequential features. Layer normalization and dropout are applied before feeding these features into the transformer. It is then processed through additional feed-forward layers before being mapped to regression and classification outputs via separate linear heads. This hybrid LSTM-transformer model effectively models temporal relationships and captures nuanced patterns in space weather data, leading to improved prediction performance (R. Zhang et al., 2025; Cao et al., 2024).

2.2.1 Loss Function

Models are trained end-to-end using a joint loss function that integrates mean squared error (MSE) for the regression task and a binary cross-entropy combined with sigmoid activation (BCEWithLogitsLoss) for classification. Given that the distributions of flare and CME counts are primarily concentrated around zero with a substantial presence of high values, their distribution is right-skewed and heavy-tailed. To address the impact of skewed distribution, a logarithmic transformation was applied after incrementing all count values by one to avoid numerical underflow. In addition, SEP events are rare compared to non-events, leading to highly imbalanced class distribution. To address this, we incorporate the Focal loss (Lin et al., 2017) for the classification task, which is designed to mitigate the effects of class imbalance.

Formally, let $\hat{y}_{\text{reg,flare}}$ and $\hat{y}_{\text{reg,CME}}$ denote the predicted future counts for flare and CME event respectively, x the classification logits, and $y_{\text{reg,flare}}$, $y_{\text{reg,CME}}$, and $y_{\text{cls}} \in \{0, 1\}$

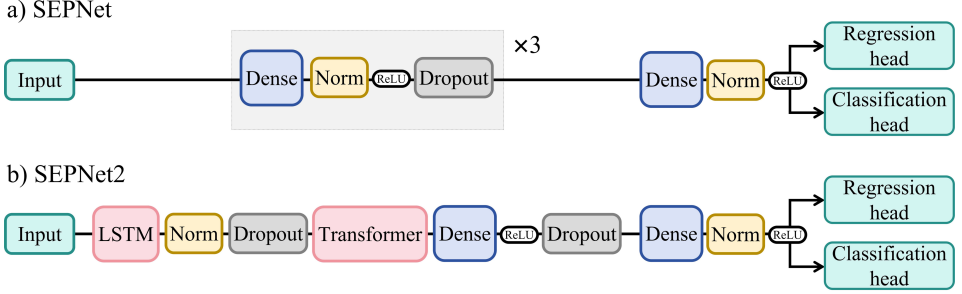


Figure 2. Diagram illustrating the architectures of the proposed multi-task learning models. **Top:** SEPNet, composed of shared feed-forward layers with layer normalization, ReLU activations, and dropout, followed by regression and classification heads for predicting flare/CME counts and SEP event probability. **Bottom:** SEPNet2, an enhanced variant introducing sequential processing via a unidirectional LSTM and transformer encoder before multi-task prediction.

represent the corresponding true targets. The overall loss function is defined as $\mathcal{L} = \mathcal{L}_{\text{MSE}} + \mathcal{L}_{\text{BCEWithLogits}} + \lambda \mathcal{L}_{\text{Focal}}$, where

$$\begin{aligned} \mathcal{L}_{\text{MSE}} &= \frac{1}{2N} \sum_{t=1}^N \left[(\log(\hat{y}_{\text{reg,flare},t} + 1) - \log(y_{\text{reg,flare},t} + 1))^2 \right. \\ &\quad \left. + (\log(\hat{y}_{\text{reg,CME},t} + 1) - \log(y_{\text{reg,CME},t} + 1))^2 \right], \\ \mathcal{L}_{\text{BCEWithLogits}} &= \frac{1}{N} \sum_{t=1}^N \left[-y_{\text{cls},t} \log \sigma(x_t) - (1 - y_{\text{cls},t}) \log(1 - \sigma(x_t)) \right], \\ \mathcal{L}_{\text{Focal}} &= \frac{1}{N} \sum_{t=1}^N \alpha (1 - \sigma(x_t))^\gamma \log \sigma(x_t). \end{aligned}$$

Here, N is the number of samples, and $\sigma(x) = 1/(1 + \exp(-x))$ is the sigmoid function converting logits x into estimated probabilities. The Focal loss hyperparameters are set by default as $\alpha = 0.25$, a balancing factor that weights the minority class more heavily, and $\gamma = 2$, a focusing parameter that adjusts the degree to which easy examples are down-weighted. As $\gamma \rightarrow 0$, the Focal loss converges to the standard cross-entropy loss. The scalar weight λ balances the contribution of the Focal loss relative to the other components and is set to 10 based on the relative scale of the losses in our experiments.

We found that training the model solely with BCEWithLogitsLoss combined with a weighted sampler leads to a relatively high false positive rate. The incorporation of Focal loss partially mitigates this issue by reducing the number of false alarms. However, we acknowledge that alternative loss formulations with more dedicated model structure may present opportunities for further optimization of predictive performance in future work.

2.2.2 Evaluation Metrics

Model performance was evaluated on the testing set using criteria routinely adopted in the space weather community, including both threshold-agnostic and event-based, confusion matrix derived metrics. Specifically, the analysis includes accuracy (ACC), area under the receiver operating characteristic curve (AUC), F1 score (threat score), probability of detection (POD, recall, hit rate), false positive rate (FPR), false alarm ratio (FAR), true skill score (TSS), and Heidke skill score (HSS). Emphasis is placed on F1, POD, TSS, and HSS, which capture core operational priorities such as sensitivity and

event-capturing skill (Leka et al., 2019). While ACC and AUC are standard for general classification, these metrics can mask important shortcomings in imbalanced-event scenarios, making confusion matrix based measures essential in SEP forecasting, where both false alarms (FP) and missed detections (FN) have significant operational implications. For statistical robustness, all metrics are aggregated across 50 random seeds to quantify model performance and variability.

Each metric is defined as follows, using true positives (TP), false positives (FP), true negatives (TN), and false negatives (FN):

$$\begin{aligned} \text{ACC} &= \frac{TP + TN}{TP + TN + FP + FN}, \\ \text{POD} &= \frac{TP}{TP + FN}, \\ \text{FPR} &= \frac{FP}{FP + TN}, \\ \text{FAR} &= \frac{FP}{TP + FP}, \\ \text{F1} &= \frac{2TP}{2TP + FP + FN}, \\ \text{TSS} &= \frac{TP}{TP + FN} - \frac{FP}{FP + TN}, \\ \text{HSS} &= \frac{2(TP \cdot TN - FP \cdot FN)}{(TP + FN)(FN + TN) + (TP + FP)(FP + TN)}. \end{aligned}$$

2.2.3 Hyperparameter Selection and Optimization

In this study, hyperparameter selection was performed using Optuna (Akiba et al., 2019), an automated optimization framework designed for efficient exploration and pruning of parameter combinations. Optuna leverages a define-by-run approach, allowing dynamic specification of search spaces and facilitating flexible experiment definition, which is particularly advantageous for neural network architectures.

Specifically, the following hyperparameters were tuned: the learning rate, which is sampled log-uniformly within $[10^{-5}, 10^{-3}]$, dictating the magnitude of parameter updates during Adam optimization; the weight decay, influencing the $L2$ regularization strength to alleviate overfitting; the dropout probability, uniformly sampled from $[0.1, 0.5]$, which further mitigates overfitting within hidden layers; and the batch size, which balances training stability with computational efficiency.

The objective function is defined on model training and returns the average training loss over repeated runs to account for stochasticity. Optuna's optimization algorithm systematically evaluates these trials and prunes unpromising candidates early, focusing resources on promising configurations. The final hyperparameter configuration corresponds to the lowest observed training loss.

Training incorporates gradient clipping, which constrains the norm of model gradients to improve stability and prevent divergence. A learning rate scheduler is utilized, reducing the learning rate when validation loss plateaus during training, supporting better convergence near optima. Additionally, early stopping is applied to halt training if no improvement in training loss is observed for an extended period, further reducing overfitting and computational cost.

3 Results

We conducted a comprehensive evaluation of SEP event prediction models, leveraging both advanced machine learning architectures and classical methods across different testing scenarios and feature combinations.

3.1 SEPVAL Dataset Evaluation

In this section, we focus on the SEPVAL testing dataset to evaluate the performance of our SEPNet model and its enhanced variant, SEPNet2, which integrates LSTM with transformer architectures. Various combinations of input features were tested, and the results are detailed in Appendix Table 2 and visualized in Figure 3. The results demonstrate that models employing SHARP parameters, either alone or combined with flare-related features, yield better predictive performance. Conversely, models relying exclusively on flare and CME features exhibit lower skill levels, with some skill scores, such as TSS and HSS, falling below zero, indicating limited capability to reliably forecast SEP events within the subsequent 24 hours.

For a rigorous comparison with the state-of-the-art pre-eruptive models (denoted as SoA) on SEPVAL, we performed 50 independent runs for each configuration to derive the median and 75th percentile (target quantile) metrics. Our models incorporating SHARP parameters generally match or outperform the SoA benchmarks in terms of standard evaluation metrics such as ACC, AUC, F1, POD, TSS, and HSS. Notably, SEPNet and SEPNet2 models with SHARP features substantially surpass the SoA models, underscoring superior capability for detecting SEP event occurrence. However, the relatively high false alarm rate highlights ongoing challenges in achieving high specificity.

In addition, we benchmarked classical machine learning techniques, including logistic regression with elastic net regularization (LR), support vector machines (SVM), random forests (RF), and extreme gradient boosting (XGB) for SEP classification tasks on the SEPVAL dataset; detailed results are provided in Appendix Table 3. Of these, the XGB model attained the best overall performance, particularly when trained on SHARP parameters alone or in combination with flare-related features. Nevertheless, these classical approaches consistently fall short of the predictive skill delivered by our proposed SEPNet architectures, underscoring the effectiveness of nonlinear and multi-task learning frameworks in this context.

3.2 Stratified Random Split Evaluation

Given the limited number of SEP events and non-events in SEPVAL, this scenario uses a random stratified split, allocating 20% of the entire dataset for testing and the remaining 80% for training. This split is repeated five times with different random seeds to ensure a robust assessment, and median metric values across the replicates are reported. This approach reaffirmed the superior performance of SEPNet models in terms of F1 score, POD, and skill scores (TSS and HSS), as presented in Figure 4 and detailed in Appendix Table 4.

For operational applicability, specifically forecasting SEP events with proton fluxes exceeding 10 pfu at energies > 10 MeV, the model was first trained on all general SEP events in the training dataset. The decision threshold for distinguishing operational SEP events was then re-optimized by maximizing the HSS, using the operational SEP labeled training data as a validation set. In the testing phase, operational SEP events were used as the reference labels, and the performance of the threshold recalibrated (re-validated) models was compared with that of the original models on the same testing dataset.

From the previous analysis, SHARP parameters combined with flare features were found to provide a suitable input set for general SEP prediction, and this feature com-

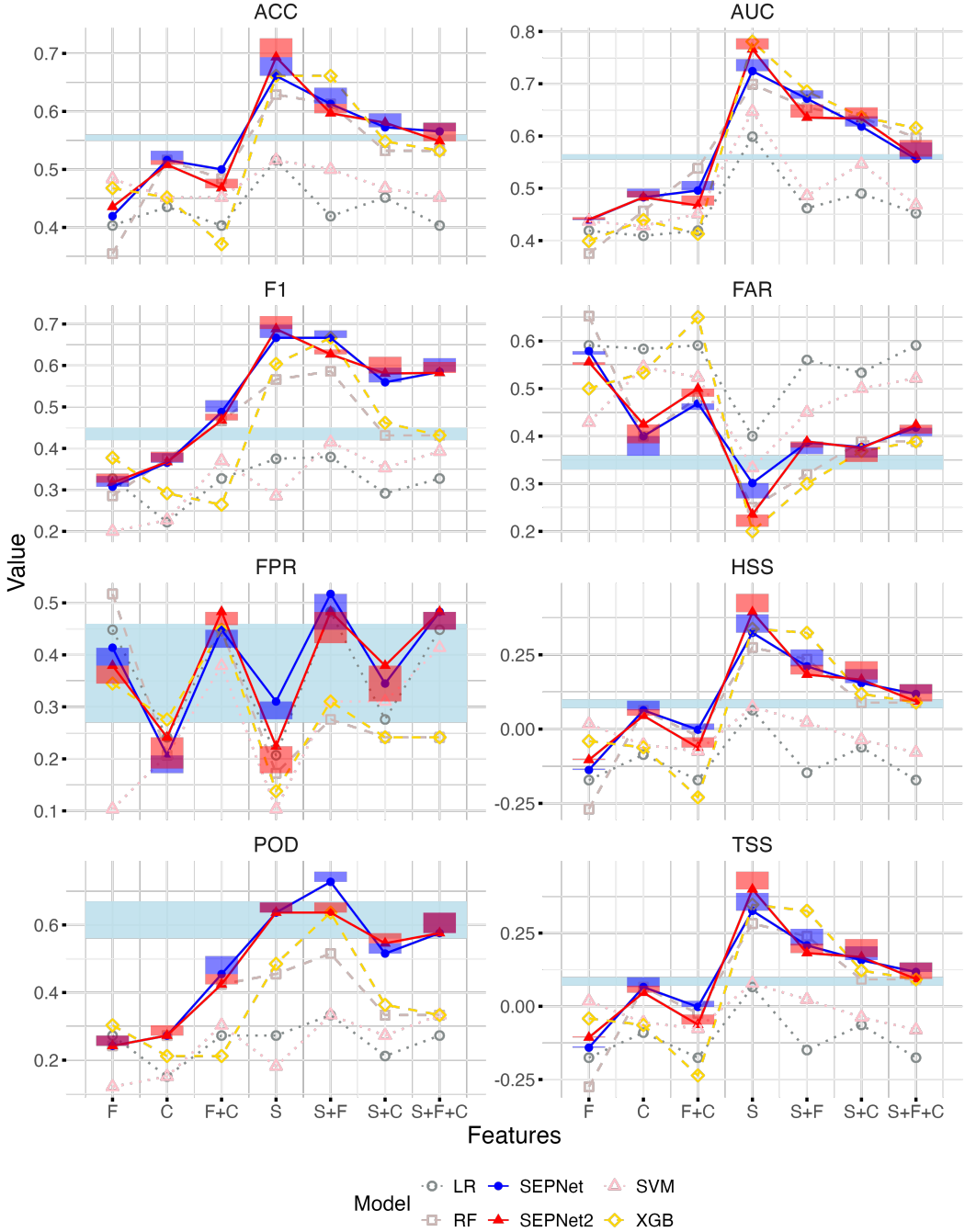


Figure 3. Performance metrics for SEPVAL prediction models, showing the median and target quantile values across different feature sets and model architectures. The shaded light blue region represents the median and target quantile achieved by state-of-the-art pre-eruption models. Feature set abbreviations: F = flare-related features; S = SHARP parameters; C = CME-related features. Performance metric abbreviations: ACC = accuracy; AUC = area under the curve; FPR = false positive rate; F1 = F1 score; POD = probability of detection; FAR = false alarm rate; TSS = true skill score; HSS = Heidke skill score. Model abbreviations: LR = logistic regression with elastic net regularization; SVM = support vector machines; RF = random forests; XGB = extreme gradient boosting.

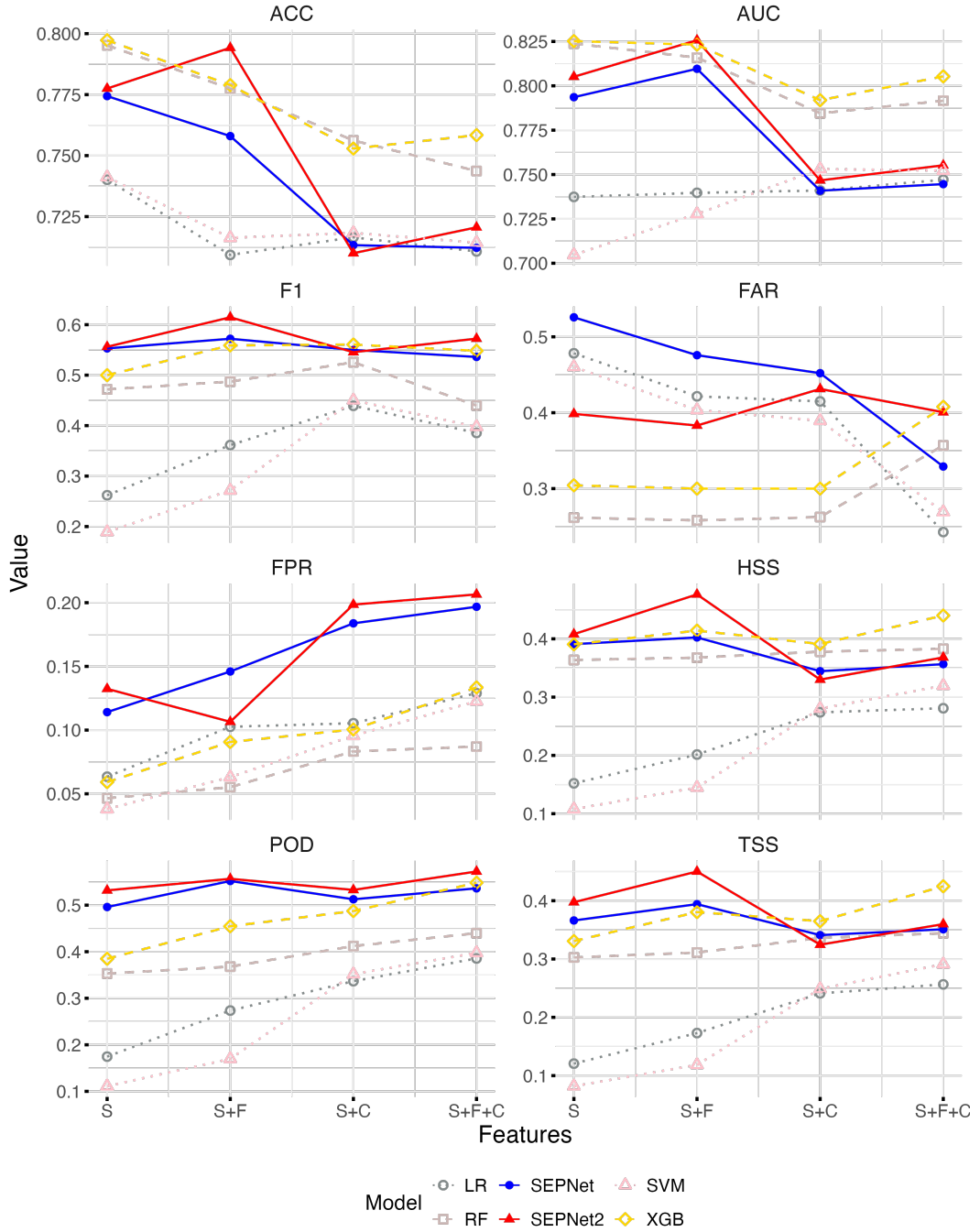


Figure 4. Performance metrics on the 20% testing set for different feature sets and models, targeting classification of general SEP events. Results for each criterion are the median values across five independent random stratified data splits. Feature set abbreviations: F = flare-related features; S = SHARP parameters; C = CME-related features. Performance metric abbreviations: ACC = accuracy; AUC = area under the curve; FPR = false positive rate; F1 = F1 score; POD = probability of detection; FAR = false alarm rate; TSS = true skill score; HSS = Heidke skill score. Model abbreviations: LR = logistic regression with elastic net regularization; SVM = support vector machines; RF = random forests; XGB = extreme gradient boosting.

bination is therefore adopted here for evaluating operational SEP performance. In this context, SEPNet2 is compared with several classical machine learning models using the re-validation strategy, with results summarized in Appendix Table 5 and partially visualized in Figure 5. SEPNet2 exhibits greater robustness with only modest changes in the performance criteria, while achieving comparatively higher AUC, lower FPR, and improved HSS. For operational SEP events, SEPNet2 attains an accuracy close to 0.8 and a TSS of approximately 0.36, indicating competitive skill in distinguishing operational SEP events from non-SEP intervals.

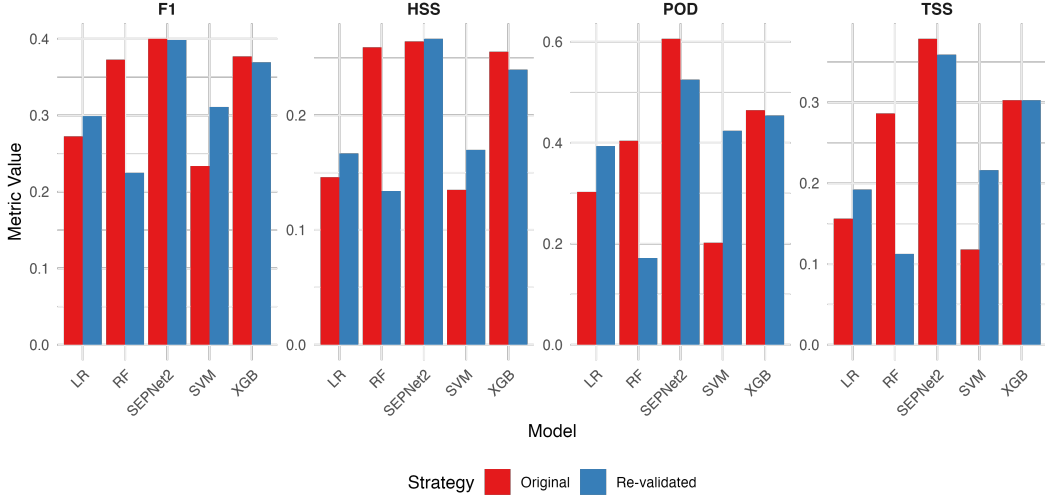


Figure 5. Performance of re-validated models (optimize the decision threshold for operational SEP event prediction) compared to original models, targeting classification of operational SEP events. Metrics are derived on the 20% testing set using SHARP parameters with flare features, with results for each criterion being the median values across five independent random stratified data splitting. Performance metric abbreviations: F1 = F1 score; POD = probability of detection; TSS = true skill score; HSS = Heidke skill score. Model abbreviations: LR = logistic regression with elastic net regularization; SVM = support vector machines; RF = random forests; XGB = extreme gradient boosting.

3.3 Real-time Forecasting

In this section, we focus on the operational challenge of real-time forecasting for SEP events expected in the months following the latest entry of the CLEAR SEP benchmark dataset. All data collected up to 10 September 2025 were used for model training, which was then applied in an operational setting. For evaluation, we employed the most recent flare observational features, combined with SHARP parameters, spanning from 23 October to 15 November 2025. It is important to note, however, that the SHARP parameters available in near-real-time differ from the definitive HARP data used during training (see the detailed information in <http://jsoc.stanford.edu/doc/data/hmi/sharp/sharp.htm>). Additionally, discrepancies in the alignment between SHARP active region designations and the corresponding flare events may result in systematic underestimation of future flare event counts. Such mismatches exemplify typical complications in real-time space weather forecasting, as highlighted in previous studies, e.g., Bobra and Couvidat (2015) and Leka et al. (2019).

For model development, we adopted the general SEP definition encompassing all events for initial training. A subsequent validation step employed the more restrictive operational SEP definition to determine an appropriate decision threshold, optimizing HSS for operational SEP event classification. The experiment was repeated 50 times to account for statistical variability. In each repetition, an optimal decision threshold was recalibrated to improve classification accuracy. The right panel of Figure 6 therefore shows the median forecast probabilities with their 25th and 75th percentiles, and the estimated probability of an operational SEP event inferred from the recalibrated threshold. The resulting binary predictions are consistent with the median of the probabilistic SEP warnings, indicating that the thresholding strategy is compatible with the underlying probability estimates.

Despite the inherent discrepancies between training and real-time datasets, SEP-Net2 reproduces the temporal patterns of future flare and CME occurrences reasonably well and issues SEP warning probabilities for active intervals during 10-14 November (see the event list at <https://sep.ccmc.gsfc.nasa.gov/events.html>), as illustrated in Figure 6. Consistent with earlier findings, there remains a tendency toward heightened false alarm rates, most notably around 1 November, when predicted SEP risk was elevated in parallel with marked flare activity. Improving the precision of SEP warnings, particularly by reducing false positives while maintaining sensitivity, will be a priority for future model development and operational deployment.

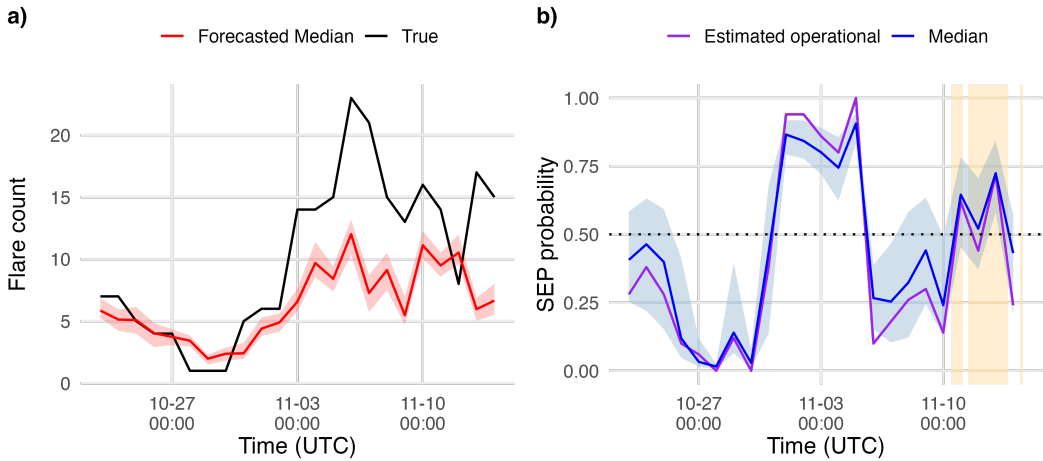


Figure 6. Forecast performance for flare counts and SEP event probabilities over the most recent 23-day period. **Left panel:** The black curve indicates observed flare counts, while the red curve shows the median forecast with shaded regions representing the interquartile range (25th to 75th percentiles). **Right panel:** The blue curve corresponds to the forecasted median SEP event probability and the purple line indicates the estimated operational SEP probability based on the calibrated decision threshold, with the shaded blue region showing the interquartile range, and orange bands mark identified SEP event intervals.

4 Discussion

This study advances the field of space weather forecasting by demonstrating the efficacy of multi-task learning and deep neural architectures for predicting SEP events. Our approach integrates solar flares, CMEs, and SHARP magnetic field parameters, enabling the models to capture the complex interactions intrinsic to SEP generation. Evaluation against classical binary classifiers across multiple input feature sets, demonstrates

that the combination of flare and SHARP magnetic features yields superior predictive performance for SEP events in the next 24 hours. The findings indicate that models incorporating SHARP parameters, either alone or in combination with flare features, achieve the highest predictive skill, as reflected in F1 scores, POD, and skill scores (TSS and HSS).

A challenge across all scenarios is the inherent class imbalance; SEP events are rare relative to non-events, which constrains POD and skill score performance. While the multi-task SEPNet models outperform classical machine learning methods and often match or exceed SoA empirical benchmarks, one limitation remains: the relatively high FAR. This reflects a tendency for models to make overpredictions, which, although increasing sensitivity, can reduce operational trust and create unnecessary caution. Addressing this issue will require exploring additional strategies for specificity enhancement, such as more diverse feature integration and recalibration against operational thresholds. Future improvements will likely derive from further dataset extension, augmentation, and integration of additional solar wind and interplanetary environment features. More sophisticated neural architectures (e.g., meta-learning, ensemble methods) and robust augmentation techniques could also yield better generalization and reliability for operational deployment.

From an operational perspective, the demonstrated ability of our models to jointly forecast SEP occurrence and the associated flare and CME activity rates within the subsequent 24-hour window offers additional predictive nuance for space weather mitigation, which will be further assessed under real-time conditions. While the present work does not explicitly predict SEP peak flux or fluence, the multi-output framework could be extended in future to incorporate event magnitude as an additional target, with potential utility for scheduling satellite operations, astronaut extravehicular activities, power grid reconfiguration, and aviation route planning.

5 Conclusion

In summary, our results highlight the power and promise of modern machine learning, particularly multi-task neural networks incorporating sequential dynamics for space weather prediction. By leveraging rich, multi-source solar activity data and advanced feature integration strategies, our models deliver robust, timely forecasts of SEP events, flares, and CMEs. Continued progress will depend on broadening training datasets, incorporating new physical observables, and refining model architectures to simultaneously maximize event detection sensitivity and reduce false alarms. Future extensions will focus on predicting SEP integrated flux and duration, enabling a more comprehensive forecast framework that quantifies not only event occurrence but also intensity and temporal evolution, key elements for effective space weather hazard mitigation.

Open Research Section

All data and code supporting the conclusions of this study are openly available at the SEP-Prediction GitHub repository: <https://github.com/yuyian/SEP-Prediction.git>. This repository will provide access to the SEPVAL benchmark dataset, SEPNet model implementation, and relevant analysis scripts. Users can freely access, reproduce, and build upon the research results presented in this manuscript.

Conflict of Interest disclosure

The authors declare there are no conflicts of interest for this manuscript.

Acknowledgments

This work is supported by the NASA Space Weather Center of Excellence program under award No. 80NSSC23M0191 and No. 80NSSC23M0192.

Appendix: Supplementary Results and Model Evaluations

This appendix provides detailed performance metrics of our proposed SEP forecasting models and benchmark classification machine learning algorithms on the SEP-VAL and stratified random split testing datasets. Tabulated median scores and target quantiles across various input feature combinations and model architectures are summarized in Tables 2, 3, 4, and 5. These results support the main analyses, offering transparency and additional insights into the robustness of SEPNet and SEPNet2, feature importance, and comparative performance under different training and testing scenarios.

Table 2. SEPVAL performance metrics: Median and target quantile across different feature sets and models.

Features	Model	ACC	AUC	FPR	F1	POD	FAR	TSS	HSS
	SoA	0.55, 0.56	0.56, –	0.46, 0.27	0.42, 0.45	0.56, 0.67	0.36, 0.33	0.07, 0.10	0.07, 0.10
F	SEPNet	0.4194, 0.4194	0.4394, 0.4420	0.4138, 0.3793	0.3077, 0.3333	0.2424, 0.2727	0.5789, 0.5714	-0.1411, -0.1369	-0.1376, -0.1330
	SEPNet2	0.4355, 0.4355	0.4404, 0.4451	0.3793, 0.3448	0.3137, 0.3396	0.2424, 0.2727	0.5556, 0.5500	-0.1066, -0.1024	-0.1038, -0.0993
C	SEPNet	0.5161, 0.5323	0.4828, 0.4990	0.2069, 0.1724	0.3655, 0.3892	0.2727, 0.2727	0.4000, 0.3588	0.0658, 0.0993	0.0634, 0.0956
	SEPNet2	0.5081, 0.5161	0.4828, 0.4948	0.2414, 0.1810	0.3673, 0.3919	0.2727, 0.3030	0.4248, 0.3846	0.0465, 0.0700	0.0450, 0.0672
F+C	SEPNet	0.5000, 0.5000	0.4958, 0.5138	0.4483, 0.4138	0.4878, 0.5161	0.4545, 0.5076	0.4688, 0.4552	-0.0021, 0.0188	-0.0021, 0.0184
	SEPNet2	0.4677, 0.4839	0.4671, 0.4864	0.4828, 0.4569	0.4677, 0.4836	0.4242, 0.4545	0.5000, 0.4828	-0.0627, -0.0282	-0.0623, -0.0280
S	SEPNet	0.6613, 0.6935	0.7241, 0.7469	0.3103, 0.2759	0.6667, 0.6981	0.6364, 0.6667	0.3015, 0.2690	0.3260, 0.3866	0.3240, 0.3858
	SEPNet2	0.6935, 0.7258	0.7659, 0.7866	0.2241, 0.1724	0.6880, 0.7189	0.6364, 0.6667	0.2354, 0.2098	0.3992, 0.4598	0.3934, 0.4550
S+F	SEPNet	0.6129, 0.6411	0.6714, 0.6873	0.5172, 0.4483	0.6667, 0.6849	0.7273, 0.7576	0.3868, 0.3623	0.2079, 0.2641	0.2110, 0.2682
	SEPNet2	0.5968, 0.6129	0.6353, 0.6604	0.4828, 0.4224	0.6269, 0.6386	0.6364, 0.6667	0.3889, 0.3758	0.1818, 0.2142	0.1833, 0.2160 _{mn}
S+C	SEPNet	0.5726, 0.5968	0.6181, 0.6377	0.3448, 0.3448	0.5594, 0.5949	0.5152, 0.5455	0.3772, 0.3548	0.1573, 0.2048	0.1549, 0.2019
	SEPNet2	0.5806, 0.6129	0.6332, 0.6549	0.3793, 0.3103	0.5806, 0.6211	0.5455, 0.5758	0.3750, 0.3456	0.1682, 0.2299	0.1665, 0.2282
S+F+	SEPNet	0.5645, 0.5806	0.5559, 0.5878	0.4828, 0.4483	0.5846, 0.6176	0.5758, 0.6364	0.4180, 0.4000	0.1170, 0.1494	0.1180, 0.1507 _{pt submitted}
C	SEPNet2	0.5484, 0.5806	0.5606, 0.5922	0.4828, 0.4483	0.5822, 0.6087	0.5758, 0.6364	0.4237, 0.4054	0.0930, 0.1494	0.0930, 0.1507

Notes: Features column abbreviations: F = flare-related features, S = SHARP parameters, C = CME-related features. Model column abbreviations: SoA = state-of-the-art pre-eruption models. Performance metric abbreviations: ACC = accuracy, AUC = area under the curve, FPR = false positive rate, F1 = F1 score, POD = probability of detection, FAR = false alarm rate, TSS = true skill score, HSS = Heidke skill score.

Table 3. SEPVAL performance metrics across different feature sets and general machine learning models.

Features	Model	ACC	AUC	FPR	F1	POD	FAR	TSS	HSS
F	LR	0.4032	0.4190	0.4483	0.3273	0.2727	0.5909	-0.1755	-0.1716
	SVM	0.4839	0.4368	0.1034	0.2000	0.1212	0.4286	0.0178	0.0168
	RF	0.3548	0.3751	0.5172	0.2857	0.2424	0.6522	-0.2748	-0.2692
	XGB	0.4677	0.3992	0.3448	0.3774	0.3030	0.5000	-0.0418	-0.0407
C	LR	0.4355	0.4091	0.2414	0.2222	0.1515	0.5833	-0.0899	-0.0861
	SVM	0.4516	0.4279	0.2069	0.2273	0.1515	0.5455	-0.0554	-0.0529
	RF	0.5161	0.4566	0.2069	0.3750	0.2727	0.4000	0.0658	0.0634
	XGB	0.4516	0.4394	0.2759	0.2917	0.2121	0.5333	-0.0637	-0.0614
F+C	LR	0.4032	0.4190	0.4483	0.3273	0.2727	0.5909	-0.1755	-0.1716
	SVM	0.4516	0.4514	0.3793	0.3704	0.3030	0.5238	-0.0763	-0.0744
	RF	0.4839	0.5381	0.4483	0.4667	0.4242	0.4815	-0.0240	-0.0237
	XGB	0.3710	0.4127	0.4483	0.2642	0.2121	0.6500	-0.2362	-0.2299
S	LR	0.5161	0.5987	0.2069	0.3750	0.2727	0.4000	0.0658	0.0634
	SVM	0.5161	0.6468	0.1034	0.2857	0.1818	0.3333	0.0784	0.0746
	RF	0.6290	0.6991	0.1724	0.5660	0.4545	0.2500	0.2821	0.2747
	XGB	0.6613	0.7806	0.1379	0.6038	0.4848	0.2000	0.3469	0.3377
S+F	LR	0.4194	0.4619	0.4828	0.3793	0.3333	0.5600	-0.1494	-0.1470
	SVM	0.5000	0.4859	0.3103	0.4151	0.3333	0.4500	0.0230	0.0224
	RF	0.6129	0.6541	0.2759	0.5862	0.5152	0.3200	0.2393	0.2354
	XGB	0.6613	0.6855	0.3103	0.6667	0.6364	0.3000	0.3260	0.3240
S+C	LR	0.4516	0.4901	0.2759	0.2917	0.2121	0.5333	-0.0637	-0.0614
	SVM	0.4677	0.5465	0.3103	0.3529	0.2727	0.5000	-0.0376	-0.0365
	RF	0.5323	0.6353	0.2414	0.4314	0.3333	0.3889	0.0920	0.0892
	XGB	0.5484	0.6364	0.2414	0.4615	0.3636	0.3684	0.1223	0.1188
S+F+C	LR	0.4032	0.4525	0.4483	0.3273	0.2727	0.5909	-0.1755	-0.1716
	SVM	0.4516	0.4681	0.4138	0.3929	0.3333	0.5217	-0.0805	-0.0788
	RF	0.5323	0.5972	0.2414	0.4314	0.3333	0.3889	0.0920	0.0892
	XGB	0.5323	0.6155	0.2414	0.4314	0.3333	0.3889	0.0920	0.0892

Notes: Features column abbreviations: F = flare-related features, S = SHARP parameters, C = CME-related features. Model column abbreviations: LR = logistic regression with elastic net penalty. SVM = support vector machine. RF = random forest. XGB = extreme gradient boosting. Performance metric abbreviations: ACC = accuracy, AUC = area under the curve, FPR = false positive rate, F1 = F1 score, POD = probability of detection, FAR = false alarm rate, TSS = true skill score, HSS = Heidke skill score.

Table 4. Performance metrics on the 20% testing set for different feature sets and models, targeting classification of general SEP events. Results for each criterion are the median values across five independent random stratified data splits.

Features	Model	ACC	AUC	FPR	F1	POD	FAR	TSS	HSS
S	LR	0.7401	0.7374	0.0634	0.2620	0.1746	0.4891	0.1206	0.1521
	SVM	0.7412	0.7047	0.0380	0.1892	0.1111	0.4754	0.0819	0.1079
	RF	0.7952	0.8238	0.0465	0.4718	0.3532	0.2727	0.3027	0.3637
	XGB	0.7973	0.8252	0.0592	0.5000	0.3849	0.2897	0.3308	0.3906
	SEPNet	0.7744	0.7936	0.1141	0.5530	0.4960	0.4201	0.3661	0.3909
	SEPNet2	0.7775	0.8051	0.1324	0.5562	0.5317	0.4174	0.3974	0.4080
S+F	LR	0.7093	0.7397	0.1026	0.3614	0.2736	0.4860	0.1730	0.2015
	SVM	0.7163	0.7278	0.0631	0.2717	0.1698	0.4512	0.1184	0.1449
	RF	0.7775	0.8159	0.0552	0.4872	0.3679	0.2602	0.3112	0.3677
	XGB	0.7789	0.8232	0.0907	0.5589	0.4547	0.3026	0.3805	0.4141
	SEPNet	0.7580	0.8096	0.1460	0.5721	0.5519	0.3967	0.3941	0.4024
	SEPNet2	0.7942	0.8257	0.1065	0.6146	0.5566	0.3140	0.4501	0.4762
S+C	LR	0.7166	0.7410	0.1054	0.4393	0.3367	0.3784	0.2411	0.2739
	SVM	0.7183	0.7531	0.0956	0.4502	0.3518	0.3750	0.2488	0.2802
	RF	0.7562	0.7845	0.0833	0.5256	0.4121	0.2844	0.3361	0.3779
	XGB	0.7529	0.7919	0.1005	0.5607	0.4874	0.3154	0.3649	0.3911
	SEPNet	0.7133	0.7409	0.1838	0.5499	0.5126	0.4327	0.3410	0.3445
	SEPNet2	0.7100	0.7467	0.1985	0.5455	0.5327	0.4378	0.3246	0.3300
S+F+C	LR	0.7107	0.7471	0.1290	0.4741	0.3855	0.3846	0.2565	0.2809
	SVM	0.7143	0.7522	0.1226	0.4981	0.3976	0.3661	0.2911	0.3196
	RF	0.7437	0.7916	0.0871	0.5455	0.4398	0.2784	0.3443	0.3828
	XGB	0.7584	0.8053	0.1335	0.6179	0.5482	0.3111	0.4248	0.4440
	SEPNet	0.7122	0.7446	0.1968	0.5686	0.5361	0.4065	0.3510	0.3565
	SEPNet2	0.7206	0.7563	0.2065	0.5802	0.5723	0.3963	0.3598	0.3681

Notes: Features column abbreviations: F = flare-related features, S = SHARP parameters, C = CME-related features. Model column abbreviations: LR = logistic regression with elastic net penalty. SVM = support vector machine. RF = random forest. XGB = extreme gradient boosting. Performance metric abbreviations: ACC = accuracy, AUC = area under the curve, FPR = false positive rate, F1 = F1 score, POD = probability of detection, FAR = false alarm rate, TSS = true skill score, HSS = Heidke skill score.

Table 5. Performance metrics on the 20% testing set using SHARP parameters with flare feature sets across different models, targeting classification of operational SEP events. Results for each criterion are the median values across five independent random stratified data splits.

	Model	ACC	AUC	FPR	F1	POD	FAR	TSS	HSS
Re-validated	LR	0.7608	0.7224	0.1903	0.2991	0.3939	0.7500	0.1922	0.1668
	SVM	0.7483	0.7181	0.2081	0.3111	0.4242	0.7544	0.2162	0.1697
	RF	0.8540	0.7720	0.0339	0.2250	0.1717	0.5750	0.1125	0.1341
	XGB	0.7955	0.7689	0.1468	0.3692	0.4545	0.6935	0.3026	0.2396
	SEPNet2	0.7914	0.7727	0.1661	0.3986	0.5253	0.6645	0.3591	0.2665
Original	LR	0.7844	0.7224	0.1419	0.2727	0.3030	0.7431	0.1563	0.1460
	SVM	0.8234	0.7181	0.0758	0.2339	0.2020	0.7121	0.1181	0.1350
	RF	0.8136	0.7720	0.1306	0.3729	0.4040	0.6549	0.2863	0.2592
	XGB	0.7733	0.7689	0.1806	0.3770	0.4646	0.6928	0.3026	0.2552
	SEPNet2	0.7524	0.7641	0.2210	0.4000	0.6061	0.7015	0.3786	0.2642

Notes: Model column abbreviations: LR = logistic regression with elastic net penalty. SVM = support vector machine. RF = random forest. XGB = extreme gradient boosting. Performance metric abbreviations: ACC = accuracy, AUC = area under the curve, FPR = false positive rate, F1 = F1 score, POD = probability of detection, FAR = false alarm rate, TSS = true skill score, HSS = Heidke skill score.

References

Akiba, T., Sano, S., Yanase, T., Ohta, T., & Koyama, M. (2019). Optuna: A next-generation hyperparameter optimization framework. In *The 25th ACM SIGKDD international conference on knowledge discovery & data mining* (pp. 2623–2631).

Ali, M. A., Abdelkawy, A. G., Shaltout, A. M., & Beheary, M. (2025). Forecasting solar energetic particles using multi-source data from solar flares, CMEs, and radio bursts with machine learning approaches. *Scientific Reports*, 15(1), 9546. doi: 10.1038/s41598-025-92207-1

Balch, C. C. (2008). Updated verification of the Space Weather Prediction Center's solar energetic particle prediction model. *Space Weather*, 6(1). Retrieved from <https://agupubs.onlinelibrary.wiley.com/doi/abs/10.1029/2007SW000337> doi: 10.1029/2007SW000337

Bobra, M. G., & Couvidat, S. (2015). Solar flare prediction using SDO/HMI vector magnetic field data with a machine-learning algorithm. *The Astrophysical Journal*, 798(2), 135. Retrieved from <http://dx.doi.org/10.1088/0004-637X/798/2/135> doi: 10.1088/0004-637X/798/2/135

Bobra, M. G., Sun, X., Hoeksema, J. T., Turmon, M., Liu, Y., Hayashi, K., ... Leka, K. D. (2014). The helioseismic and magnetic imager (HMI) vector magnetic field pipeline: SHARPs-space-weather HMI active region patches. *Solar Physics*, 289(9), 3549–3578. Retrieved from <http://dx.doi.org/10.1007/s11207-014-0529-3> doi: 10.1007/s11207-014-0529-3

Boubrahimi, S. F., Aydin, B., Martens, P., & Angryk, R. (2017). On the prediction of \gtrsim 100 MeV solar energetic particle events using GOES satellite data. In *2017 IEEE international conference on big data (big data)* (p. 2533-2542). doi: 10.1109/BigData.2017.8258212

Cao, K., Zhang, T., & Huang, J. (2024). Advanced hybrid LSTM-transformer architecture for real-time multi-task prediction in engineering systems. *Scientific Reports*, 14(1), 4890. doi: 10.1038/s41598-024-55483-x

Caruana, R. (1997). Multitask learning. *Machine learning*, 28(1), 41–75.

Community, T. S., Barnes, W. T., Bobra, M. G., Christe, S. D., Freij, N., Hayes, L. A., ... Contributors, S. (2020). The SunPy project: Open source development and status of the version 1.0 core package. *The Astrophysical Journal*, 890(1), 68. Retrieved from <https://doi.org/10.3847/1538-4357/ab4f7a> doi: 10.3847/1538-4357/ab4f7a

Crawshaw, M. (2020). Multi-task learning with deep neural networks: A survey. *ArXiv*, abs/2009.09796. Retrieved from <https://api.semanticscholar.org/CorpusID:221819295>

Dayeh, M. A., Chatterjee, S., Muñoz-Jaramillo, A., Moreland, K., Bain, H. M., & Hart, S. T. (2024). MEMPSEP-II. Forecasting the properties of solar energetic particle events using a multivariate ensemble approach. *Space Weather*, 22(9), e2023SW003697. Retrieved from <https://agupubs.onlinelibrary.wiley.com/doi/abs/10.1029/2023SW003697> doi: 10.1029/2023SW003697

Desai, M., & Giacalone, J. (2016). Large gradual solar energetic particle events. *Living Reviews in Solar Physics*, 13(1), 3. Retrieved from <https://doi.org/10.1007/s41116-016-0002-5>

Desai, M. I., Mitchell, D. G., Szalay, J. R., Roelof, E. C., Giacalone, J., Hill, M. E., ... Kasper, J. C. (2020). Properties of suprathermal-through-energetic he ions associated with stream interaction regions observed over the parker solar probe's first two orbits. *The Astrophysical Journal Supplement Series*, 246(2), 56. Retrieved from <https://doi.org/10.3847/1538-4365/ab65ef> doi: 10.3847/1538-4365/ab65ef

Eastwood, J. P., Biffis, E., Hapgood, M. A., Green, L., Bisi, M. M., Bentley, R. D., ... Burnett, C. (2017). The economic impact of space weather: Where do we stand? *Risk Analysis*, 37(2), 206-218. Retrieved from

https://onlinelibrary.wiley.com/doi/abs/10.1111/risa.12765 doi: 10.1111/risa.12765

Erickson, W. (1997). The bruny island radio spectrometer. *Publications of the Astronomical Society of Australia*, 14(3), 278–282. Retrieved from https://doi.org/10.1071/AS97278

Glogowski, K., Bobra, M. G., Choudhary, N., Amezcua, A. B., & Mumford, S. J. (2019). drms: A Python package for accessing HMI and AIA data. *Journal of Open Source Software*, 4(40), 1614. Retrieved from https://doi.org/10.21105/joss.01614 doi: 10.21105/joss.01614

Gopalswamy, N., Aguilar-Rodriguez, E., Yashiro, S., Nunes, S., Kaiser, M. L., & Howard, R. A. (2005). Type II radio bursts and energetic solar eruptions. *Journal of Geophysical Research: Space Physics*, 110(A12). Retrieved from https://agupubs.onlinelibrary.wiley.com/doi/abs/10.1029/2005JA011158 doi: 10.1029/2005JA011158

Hastie, T., Tibshirani, R., & Friedman, J. (2009). *The Elements of Statistical Learning: Data Mining, Inference, and Prediction*. Springer. Retrieved from https://books.google.com/books?id=eBSgoAEACAAJ

Hilberg, R. (1969). *Radiation protection for apollo missions-case 340*. Retrieved from https://www.lpi.usra.edu/lunar/documents/NTRS/collection3/NASA_CR_106949.pdf

Hochreiter, S., & Schmidhuber, J. (1997, 11). Long short-term memory. *Neural Computation*, 9(8), 1735–1780. Retrieved from https://doi.org/10.1162/neco.1997.9.8.1735 doi: 10.1162/neco.1997.9.8.1735

Hu, J., Li, G., Ao, X., Zank, G. P., & Verkhoglyadova, O. (2017). Modeling particle acceleration and transport at a 2-D CME-driven shock. *Journal of Geophysical Research: Space Physics*, 122(11), 10,938–10,963. Retrieved from https://agupubs.onlinelibrary.wiley.com/doi/abs/10.1002/2017JA024077 doi: 10.1002/2017JA024077

Iucci, N., Levitin, A. E., Belov, A. V., Eroshenko, E. A., Ptitsyna, N. G., Villoresi, G., ... Yanke, V. G. (2005). Space weather conditions and spacecraft anomalies in different orbits. *Space Weather*, 3(1). Retrieved from https://agupubs.onlinelibrary.wiley.com/doi/abs/10.1029/2003SW000056 doi: 10.1029/2003SW000056

Ji, A., Patil, P., Pandey, C., Georgoulis, M. K., & Aydin, B. (2025). *Enhancing explainability in solar energetic particle event prediction: A global feature mapping approach*. Retrieved from https://arxiv.org/abs/2511.09475

Jiao, Z., Sun, H., Wang, X., Manchester, W., Gombosi, T., Hero, A., & Chen, Y. (2020). Solar flare intensity prediction with machine learning models. *Space Weather*, 18(7), e2020SW002440. Retrieved from https://agupubs.onlinelibrary.wiley.com/doi/abs/10.1029/2020SW002440 doi: 10.1029/2020SW002440

Kasapis, S., Zhao, L., Chen, Y., Wang, X., Bobra, M., & Gombosi, T. (2022). Interpretable machine learning to forecast SEP events for solar cycle 23. *Space Weather*, 20(2), e2021SW002842. Retrieved from https://agupubs.onlinelibrary.wiley.com/doi/abs/10.1029/2021SW002842 doi: 10.1029/2021SW002842

Kim, M.-H. Y., De Angelis, G., & Cucinotta, F. A. (2011). Probabilistic assessment of radiation risk for astronauts in space missions. *Acta Astronautica*, 68(7), 747–759. Retrieved from https://www.sciencedirect.com/science/article/pii/S0094576510003231 doi: 10.1016/j.actaastro.2010.08.035

Klein, K.-L., & Dalla, S. (2017). Acceleration and propagation of solar energetic particles. *Space Science Reviews*, 212(3), 1107–1136. Retrieved from https://doi.org/10.1007/s11214-017-0382-4

Laurenza, M., Cliver, E. W., Hewitt, J., Storini, M., Ling, A. G., Balch, C. C., & Kaiser, M. L. (2009). A technique for short-term warning of solar energetic

particle events based on flare location, flare size, and evidence of particle escape. *Space Weather*, 7(4). Retrieved from <https://agupubs.onlinelibrary.wiley.com/doi/abs/10.1029/2007SW000379> doi: 10.1029/2007SW000379

Lavasa, E., Giannopoulos, G., Papaioannou, A., Anastasiadis, A., Daglis, I., Aran, A., ... Sanahuja, B. (2021). Assessing the predictability of solar energetic particles with the use of machine learning techniques. *Solar Physics*, 296(7), 107. Retrieved from <https://doi.org/10.1007/s11207-021-01837-x>

Leka, K. D., Park, S.-H., Kusano, K., Andries, J., Barnes, G., Bingham, S., ... Terkildsen, M. (2019, aug). A comparison of flare forecasting methods. ii. benchmarks, metrics, and performance results for operational solar flare forecasting systems. *The Astrophysical Journal Supplement Series*, 243(2), 36. Retrieved from <https://doi.org/10.3847/1538-4365/ab2e12> doi: 10.3847/1538-4365/ab2e12

Lin, T.-Y., Goyal, P., Girshick, R., He, K., & Dollár, P. (2017). Focal loss for dense object detection. In *Proceedings of the ieee international conference on computer vision (iccv)* (pp. 2980–2988).

Liu, C., Deng, N., Wang, J. T. L., & Wang, H. (2017). Predicting solar flares using SDO/HMI vector magnetic data products and the random forest algorithm. *The Astrophysical Journal*, 843(2), 104. Retrieved from <https://doi.org/10.3847/1538-4357/aa789b> doi: 10.3847/1538-4357/aa789b

Liu, W., Gombosi, T., Sokolov, I., & Zhao, L. (2025). Not all shocks are created equal: Shock acceleration during the 2013 April 11 solar energetic particle event. In *European geosciences union general assembly 2025, egu25*. Vienna, Austria. Retrieved from <https://doi.org/10.5194/egusphere-egu25-3351> (EGU25-3351) doi: 10.5194/egusphere-egu25-3351

Luhmann, J., Ledvina, S., Krauss-Varban, D., Odstrcil, D., & Riley, P. (2007). A heliospheric simulation-based approach to SEP source and transport modeling. *Advances in Space Research*, 40(3), 295-303. Retrieved from <https://www.sciencedirect.com/science/article/pii/S0273117707003419> doi: 10.1016/j.asr.2007.03.089

Neergaard Parker, L., & Zank, G. P. (2012). Particle acceleration at quasi-parallel shock waves: Theory and observations at 1 AU. *The Astrophysical Journal*, 757(1), 97. Retrieved from <https://doi.org/10.1088/0004-637X/757/1/97> doi: 10.1088/0004-637X/757/1/97

Opgenoorth, Hermann J., Wimmer-Schweingruber, Robert F., Belehaki, Anna, Berghmans, David, Hapgood, Mike, Hesse, Michael, ... Temmer, Manuela (2019). Assessment and recommendations for a consolidated european approach to space weather – as part of a global space weather effort. *Journal of Space Weather and Space Climate*, 9, A37. Retrieved from <https://doi.org/10.1051/swsc/2019033> doi: 10.1051/swsc/2019033

Reames, D. (2004). Solar energetic particle variations. *Advances in Space Research*, 34(2), 381-390. Retrieved from <https://www.sciencedirect.com/science/article/pii/S0273117704002406> (Solar Variability and Climate Change) doi: 10.1016/j.asr.2003.02.046

Richardson, I., Von Rosenvinge, T., Cane, H., Christian, E., Cohen, C., Labrador, A., ... Stone, E. (2014). \sim 25 MeV proton events observed by the high energy telescopes on the STEREO A and B spacecraft and/or at Earth during the first seven years of the STEREO mission. *Solar Physics*, 289(8), 3059–3107.

Sandnes, A. T., Grimstad, B., & Kolbjørnsen, O. (2024). Multi-task neural networks by learned contextual inputs. *Neural Networks*, 179, 106528. Retrieved from <https://www.sciencedirect.com/science/article/pii/S0893608024004520> doi: 10.1016/j.neunet.2024.106528

Smart, D., & Shea, M. (1979). Pps76: A computerized event mode solar proton forecasting technique. In *Noaa solar-terrestrial predictions proceedings* (Vol. 1, pp. 406–427).

Sokolov, I. V., Roussev, I. I., Gombosi, T. I., Lee, M. A., Kóta, J., Forbes, T. G., ... Sakai, J. I. (2004, oct). A new field line advection model for solar particle acceleration. *The Astrophysical Journal*, 616(2), L171. Retrieved from <https://doi.org/10.1086/426812> doi: 10.1086/426812

Tylka, A. J., & Lee, M. A. (2006). A model for spectral and compositional variability at high energies in large, gradual solar particle events. *The Astrophysical Journal*, 646(2), 1319. Retrieved from <https://doi.org/10.1086/505106> doi: 10.1086/505106

Vaswani, A., Shazeer, N., Parmar, N., Uszkoreit, J., Jones, L., Gomez, A. N., ... Polosukhin, I. (2023). *Attention is all you need*. Retrieved from <https://arxiv.org/abs/1706.03762>

Wang, R., & Sun, K. (2024). *TIMIT speaker profiling: A comparison of multi-task learning and single-task learning approaches*. Retrieved from <https://arxiv.org/abs/2404.12077>

Whitman, K. (2025a). *Fetchsep: Tools for identifying solar energetic particle events*. <https://github.com/ktindiana/fetchsep>. (Accessed: 2025-12-01)

Whitman, K. (2025b). *SEPVAL 2023 challenge event lists (v2)*. Zenodo. Retrieved from <https://doi.org/10.5281/zenodo.15555244> doi: 10.5281/zenodo.15555244

Whitman, K., & Collaboration, S. (2024). *SEPVAL 2023: SEP model validation working meeting – final results*. NASA Technical Reports Server. (<https://ccmc.gsfc.nasa.gov/challenges/sep/>)

Whitman, K., Egeland, R., Quinn, P., Stegeman, L., Allison, C., Dierckxsens, M., ... Bain, H. (2024). A multi-year effort to forward the validation of solar energetic particle models. In *Triennial earth-sun summit*.

Whitman, K., Egeland, R., Richardson, I. G., Allison, C., Quinn, P., Barzilia, J., ... Hosseinzadeh, P. (2023). Review of solar energetic particle prediction models. *Advances in Space Research*, 72(12), 5161-5242. Retrieved from <https://www.sciencedirect.com/science/article/pii/S0273117722007244> doi: 10.1016/j.asr.2022.08.006

Winter, L. M., & Balasubramaniam, K. (2015). Using the maximum x-ray flux ratio and x-ray background to predict solar flare class. *Space Weather*, 13(5), 286-297. Retrieved from <https://agupubs.onlinelibrary.wiley.com/doi/abs/10.1002/2015SW001170> doi: 10.1002/2015SW001170

Wu, S., Zhang, H. R., & Ré, C. (2020). Understanding and improving information transfer in multi-task learning. In *International conference on learning representations*. Retrieved from <https://openreview.net/forum?id=SylzhkBtDB>

Zhang, R., Bu, S., Zheng, Y., Li, G., Wan, X., Zeng, Q., & Zhou, M. (2025). A novel multi-task learning model based on Transformer-LSTM for wind power forecasting. *International Journal of Electrical Power & Energy Systems*, 169, 110732. Retrieved from <https://www.sciencedirect.com/science/article/pii/S0142061525002832> doi: 10.1016/j.ijepes.2025.110732

Zhang, Y., & Yang, Q. (2017, 09). An overview of multi-task learning. *National Science Review*, 5(1), 30-43. Retrieved from <https://doi.org/10.1093/nsr/nwx105> doi: 10.1093/nsr/nwx105

Zhao, L. (2023). *CLEAR space weather center of excellence: All-clear solar energetic particle prediction*. Retrieved from <https://arxiv.org/abs/2310.14677>

Zou, D., Cao, Y., Zhou, D., & Gu, Q. (2020). Gradient descent optimizes over-parameterized deep relu networks. *Machine learning*, 109(3), 467–492. doi: 10.1007/s10994-019-05839-6